Model-based distortion correction for Magnetic Resonance Echo Planar Imaging

Sudhanya Chatterjee[1] SUDHANYA.CHATTERJEE@GEHEALTHCARE.COM
Florian Wiesinger[2] FLORIAN.WIESINGER@GEHEALTHCARE.COM
Patricia Lan[3] PATRICIA.LAN@GEHEALTHCARE.COM
Rajagopalan Sundaresan[1] RAJAGOPALAN.SUNDARESAN@GEHEALTHCARE.COM
Dattesh Shanbhag[1] DATTESH.SHANBHAG@GEHEALTHCARE.COM
Arnaud Guidon[4] ARNAUD.GUIDON@GEHEALTHCARE.COM
[1] *GE HealthCare, Banglore, India*
[2] *GE HealthCare, Munich, Germany*
[3] *GE HealthCare, Menlo Park, CA, USA*
[4] *GE HealthCare, Boston, MA, USA*

Editors: Under Review for MIDL 2026

Abstract

Echo planar imaging (EPI) enables rapid magnetic resonance (MR) imaging and is widely used in applications such as diffusion-weighted imaging (DWI) and functional MRI (fMRI). However, EPI is highly susceptible to geometric distortion artifacts, which degrade image quality and hinder accurate diagnosis. In this work, we propose a reconstruction framework that leverages AI-learned priors within a model-based approach to correct EPI distortions. The method was evaluated on multiple in-vivo MRI datasets, including phantom, brain, and prostate diffusion-weighted imaging. Experimental results demonstrate the effectiveness of the proposed technique in mitigating distortion artifacts, thereby improving the reliability of EPI-based imaging.

Keywords: EPI, distortion correction, model based, field inhomogeneities, unrolled.

1. Introduction

Echo planar imaging (EPI) is a widely used MRI technique because it enables rapid image acquisition, making it particularly valuable for applications such as diffusion-weighted imaging (DWI) and functional MRI (fMRI). However, EPI is highly susceptible to geometric distortions caused by phase errors arising from magnetic field inhomogeneities, which can pose significant diagnostic challenges. Intensity artifacts due to signal pileup or dilution compromise tissue texture and contrast in corrected images or introduces blur in corrected image (Andersson et al., 2003; Holland et al., 2010; Zaid Alkilani et al., 2024). Although EPI distortion correction has been pursued extensively, these methods face limitations such as residual distortions post correction due to imperfections in field map (Jezzard and Balaban, 1995; Holland et al., 2010). These methods struggle when distortion is extreme resulting in non-physical tissue wraps post correction (Andersson et al., 2003).

Numerous strategies have been proposed in the literature to address these distortions.(Munger et al., 2000) introduced a distortion reduction technique by solving EPI imaging equations using conjugate gradient algorithms. (Yarach et al., 2017) developed a model-based iterative approach to correct distortions in single-shot EPI data acquired at 7T. More recently,

several deep learning-based methods have also been proposed to mitigate EPI distortions (Zaid Alkilani et al., 2024; Ge et al., 2024). Inspired from (Pruessmann et al., 1999), (Yeung et al., 2025) recently demonstrated a model-based approach to EPI distortion correction by creating an encoding matrix that captures the effect of field inhomogeneities and applying advanced algebraic methods to obtain the distortion-free image. While there has been model-based and deep learning (DL) based efforts which have been pursued for EPI distortion correction, a tighter integration between both method (more unified approach) remains an open area of investigation.

In this work, we propose a model-based distortion correction for EPI MRI regularized with deep-learning (DL) priors. We first establish a forward signal model for distortion correction, following (Yeung et al., 2025). Rather than solving the problem purely within a model-based framework, we implement an unrolled DL-based reconstruction to estimate the distortion-corrected EPI images. To facilitate clinical adoption, the method relies on a pair of EPI acquisitions with opposite phase-encoding polarity (blip-up/blip-down). This acquisition strategy for EPI distortion correction is well established (Chang and Fitzpatrick, 1992; Morgan et al., 2004) and is widely available in routine clinical protocols, which simplifies deployment of the proposed approach. The opposite-polarity images are used to estimate the off-resonance field (ΔB_0) with a DL network. The estimated field is then incorporated into the encoding matrix, which models the effect of field inhomogeneities on the measured signal. The resulting inverse problem is solved using the unrolled DL reconstruction, yielding distortion-corrected images. We demonstrate the method on phantom data and in vivo data across multiple anatomies. The results indicate that the proposed approach effectively corrects EPI distortions and generalizes across anatomies without fine-tuning.

2. Method

2.1. Signal Model

The signal modeling and notation in this work are inspired by (Bernstein et al., 2004; Brown et al., 2014; Pruessmann et al., 1999). Let the observed k-space data be denoted by Y and the distortion-free image by X. In our setting, Y is the k-space representation of an MR image affected by ΔB_0–related geometric distortions. Our objective is to estimate the artifact-free image X. In the absence of any ΔB_0 artifacts, X and Y are related by the Cartesian Fourier encoding operator. Using the discrete Fourier transform (DFT) convention, the forward model is as follows:

$$Y[k_x, k_y] = \sum_{n_x=0}^{N_x-1} \sum_{n_y=0}^{N_y-1} X[n_x, n_y] \exp\left(-i\,2\pi\left(\frac{k_x n_x}{N_x} + \frac{k_y n_y}{N_y}\right)\right). \tag{1}$$

Vectorizing both sides yields: $\mathrm{vec}(Y) = \mathbf{F}_{2\mathrm{D}}\,\mathrm{vec}(X)$, $\mathbf{F}_{2\mathrm{D}} = \mathbf{F}_y \otimes \mathbf{F}_x$, with matrix elements

$$(\mathbf{F}_x)_{k_x,n_x} = \exp\left(-i\,2\pi\,\frac{k_x n_x}{N_x}\right), \quad (\mathbf{F}_y)_{k_y,n_y} = \exp\left(-i\,2\pi\,\frac{k_y n_y}{N_y}\right), \tag{2}$$

and, equivalently,

$$\left(\mathbf{F}_{2\mathrm{D}}\right)_{(k_x,k_y),(n_x,n_y)} = \exp\left[-i\,2\pi\left(\frac{k_x n_x}{N_x} + \frac{k_y n_y}{N_y}\right)\right]. \tag{3}$$

Here, $X[n_x, n_y] \in \mathbb{C}$ denotes the complex image (spin density) at voxel indices $n_x \in \{0, \ldots, N_x - 1\}$ and $n_y \in \{0, \ldots, N_y - 1\}$; $Y[k_x, k_y] \in \mathbb{C}$ denotes k-space samples on a Cartesian grid with frequency indices $k_x \in \{0, \ldots, N_x - 1\}$ and $k_y \in \{0, \ldots, N_y - 1\}$. The integers N_x and N_y are the image dimensions along x and y, respectively; i is the imaginary unit; vec$(\cdot)$ stacks array entries with the x-index varying fastest (row-major order); and $\otimes$ denotes the Kronecker product.

B_0 off-resonance. We incorporate static field inhomogeneity via a voxelwise frequency offset $\Delta\omega[n_x, n_y] \triangleq \gamma\, \Delta B_0[n_x, n_y]$ (rad/s), where γ is the gyromagnetic ratio and $\Delta B_0[n_x, n_y]$ (T) denotes the local deviation from the nominal field at voxel (n_x, n_y). Let $t[k_x, k_y]$ (s) be the acquisition time of the k-space sample indexed by (k_x, k_y), measured relative to a reference (e.g., echo center). Under Cartesian sampling, the forward model in the presence of off-resonance becomes

$$Y[k_x, k_y] = \sum_{n_x=0}^{N_x-1} \sum_{n_y=0}^{N_y-1} X[n_x, n_y] \exp\left(-i\, 2\pi \left(\frac{k_x n_x}{N_x} + \frac{k_y n_y}{N_y}\right)\right) \exp\big(i\, \Delta\omega[n_x, n_y]\, t[k_x, k_y]\big).$$

Vectorizing yields $\text{vec}(Y) = \big(\mathbf{F}_{2\text{D}} \odot \mathbf{\Psi}\big)\, \text{vec}(X)$. Henceforth, we shall refer to $\mathbf{F}_{2\text{D}} \odot \mathbf{\Psi}$ as E, where $\odot$ denotes the Hadamard (element-wise) product.. Here $\mathbf{\Psi}_{(k_x,k_y),(n_x,n_y)} = \exp\big(i\, \Delta\omega[n_x, n_y]\, t[k_x, k_y]\big)$, i.e., the off-resonance introduces a sample- and voxel-dependent phase factor that modulates the Cartesian Fourier kernel.

Matrix Formulation Based on the above discussion, we can express the signal formation as matrix operation involving Y, X and E as $y = Ex$, where y, x are vec $(\cdot)$ version of Y, X respectively. Since E $(= \mathbf{F}_{2\text{D}} \odot \mathbf{\Psi})$ in our case depends on ΔB_0, we shall henceforth write our signal formation model as:

$$y = E\,(\Delta B_0)\, x \tag{4}$$

2.2. Solving for distortion corrected image

In this work, we approach the problem of distortion correction in EPI due to ΔB_0 inhomogeneities assuming a forward polarity and reverse polarity images is acquired (Chang and Fitzpatrick, 1992; Morgan et al., 2004). Our objective is to solve for x in Eq. 4 provided we have a forward and reverse polarity EPI MR images, denoted as $I\uparrow$ and $I\downarrow$ respectively. It shall be noted, that to populate matrix E in Eq. 4, we need to estimate ΔB_0 too. Hence, the optimization problem is as shown in Eq. 5

$$\arg\min_{x, \Delta B_0} \big\|y - E(\Delta B_0)\, x\big\|_2^2 + \lambda\, R(x) \tag{5}$$

where $R(x)$ is the regularization term and $\lambda(> 0)$ its weight. Given the nature of formulation for $E(\Delta B_0)$, it is non-trivial to solve for ΔB_0 and x simultaneously. Hence, these are solved alternatively. In the first step, we estimate the field inhomogeneity using $I\uparrow$ and $I\downarrow$. We obtain $\widehat{\Delta B_0}$ as, $\widehat{\Delta B_0} = d_\theta(I\uparrow, I\downarrow)$, $d_\theta(\cdot)$ is a convolutional neural network (CNN) with parameters θ. Let $E\Big(\widehat{\Delta B_0}\Big)$ be referred to as $\widehat{E}$ hereafter. The estimated field inhomogeneity is then used to solve for x. In our case, a quadratic form regularizer is chosen for $R(x)$. The updated optimization problem is shown below.

$$\arg\min_{x} \big\|y - \widehat{E}x\big\|_2^2 + \lambda\, \big\|x - z\big\|_2^2 \tag{6}$$

where z in Eq. 6 is a DL derived prior. The optimization problem in Eq. 6 is solved iteratively using DL derived prior. Both terms in the optimization equation are convex, hence we use a forward–backward splitting approach to solve for x.

Unit-step updates ($\tau = 1$). For the k^{th} iteration, define $f(x) = \left\|y - \widehat{E}x\right\|_2^2$ with gradient $\nabla_x f(x) = 2\,\widehat{E}^H\big(\widehat{E}x - y\big)$. Using a unit step size $\tau = 1$, the data-consistency update is as shown in Eq. 7. For more discussion on selection of $\tau = 1$, please refer to Appendix A.

$$v^{(k+1)} = x^{(k)} - \tau\,\nabla_x f\big(x^{(k)}\big) \;=\; x^{(k)} - 2\,\widehat{E}^H\Big(\widehat{E}x^{(k)} - y\Big)\,. \tag{7}$$

Provided $z^{(k)}$ is the AI learned prior for the k^{th} iteration, the proximal update for the quadratic prior (also with $\tau = 1$) is

$$x^{(k+1)} = \frac{v^{(k+1)} + 2\,\lambda\,z^{(k)}}{1 + 2\,\lambda}. \tag{8}$$

where the AI learned prior is $z^{(k)} = g_\phi^{(k)}\left(v^{(k+1)}, \Delta\widehat{B_0}\right)$; here $g_\phi^{(k)}(\cdot)$ is a CNN with ϕ trainable parameters for the k^{th} iteration.

2.3. Implementation details

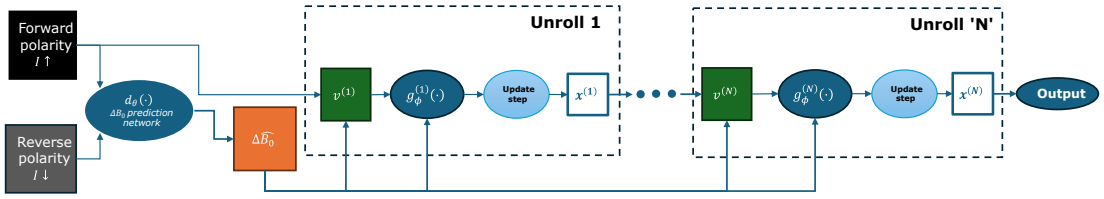

Figure 1: Illustration of the proposed model-based distortion correction for EPI MRI as discussed in Section 2.1 and 2.2.

The method's implementation has been illustrated in Figure 1. Residual channel attention network (RCAN) (Zhang et al., 2018) is used for both ΔB_0 estimation (i.e. $d_\theta(\cdot)$) and for DL prior estimation at each unrolling step (i.e. $g_\phi^{(k)}(\cdot)$). The number and RCAN {groups,blocks} used for $d_\theta(\cdot)$ and each $g_\phi^{(k)}(\cdot)$ is {5,5} and {3,3} respectively. Both RCAN networks had number of features, reduction rate and kernel size as 64, 16 and 3 respectively. Three unrolling steps were performed. Total number of trainable parameters for the network was 4.6 million. Training was performed using an Adam optimizer (learning rate of 1e-4) for 50 epochs. Inspired by (De Goyeneche Macaya et al., 2023; Muckley et al., 2021; Lebel, 2020), to avoid biasing the learning towards and contrast or structure information, the proposed method was trained on natural images (Lim et al., 2017) (Agustsson and Timofte, 2017). High-resolution patches were extracted form the images with random anchors for every training epoch. Random ΔB_0 inhomogeneity was simulated for the images (weighted by image gradients to ensure relevant distortion at boundaries). The distortion was simulated as discussed in Section 2.1.

2.4. Experiment

We evaluated the proposed method on the NIST diffusion phantom, where structures are well characterized, and on brain and pelvic data from healthy volunteers, all under IRB approval. For each dataset, we assessed distortion correction by comparing the corrected EPI MRI to T2-weighted fast spin echo (FSE) images. T2-weighted FSE is minimally affected by ΔB_0 inhomogeneities and therefore serves as a suitable reference. For fair comparison, the T2-weighted FSE images were resampled to the EPI image space to ensure coordinate alignment. The same model-based approach was used across all applications and anatomies without fine-tuning, demonstrating the method's ability to generalize.

Phantom data A NIST diffusion MRI phantom was scanned for analysis. Single-shot EPI data acquired with echo time (TE) = 80.7ms, Repetition time (TR) = 4614ms, 4mm slice thickness, 4.4mm space between slices, FOV=24cm×24cm, matrix size = 128×128, This data was acquired on a 1.5T GE HealthCare Signa Creator MRI scanner.

Brain data Single-shot EPI data acquired with TE=75.7 ms, 4.5 mm slice-thickness, FOV=24cm×24 cm, matrix size=128×128. This data was acquired on a 1.5T GE HealthCare Signa Creator MRI scanner.

Prostate data Three shots acquired with TE=63.4ms, TR=2780ms, 4.2mm slice thickness, FOV =26cmx26cm, matrix=168x168, diffusion direction=ALL, b50 (4 NEX) and b800 (8 NEX), ASSET R=1. This data was acquired on a 3T GE HealthCare SIGNA Premier MRI system.

3. Results and Discussion

Figure 2 illustrates the effectiveness of the proposed method in mitigating EPI-induced distortions and restoring geometric fidelity. This is demonstrated in corrected images which accurately recover the structural shapes observed in T2 FSE scans, without any residual distortion, in both the internal phantom structures (See circles and arrows) and the overall phantom contour. Another example from this scan is shown in Appendix B, Figure 7.

In anatomical imaging, we demonstrate the effectiveness of the proposed method to restore the structural and signal integrity of EPI images in two anatomical regions (brain and prostate) typically impacted by distortion due to air-induced susceptibility gradients. Figure 3 demonstrates that distortion induced in brain around the sinus regions (slices a-f) are restored with proposed method and maintain good congruency with structure contour obtained on reference T2w images and extremely minimal residual distortion. The sagittal view (refer Figure 4) provides better estimate of the tissue distortion adjacent to sinuses (and pons) and associated signal pileup. Notice that proposed method provides reliable distortion correction while maintaining integrity of tissue texture and contrast despite signal pileup. This is important for ensuring reliable tissue characterization with DWI images without obscuring the view of any underlying lesion.

Similarly in prostate imaging, distortion due to rectal gas is common and results in DWI imaging being not readable and hinders adoption of PIRADS standard for tumor assessment. We notice that the proposed method has completely restored the EPI distortion uniformly in rectal gas region (Figure 6) across the slices in ano-rectal region without any impact of

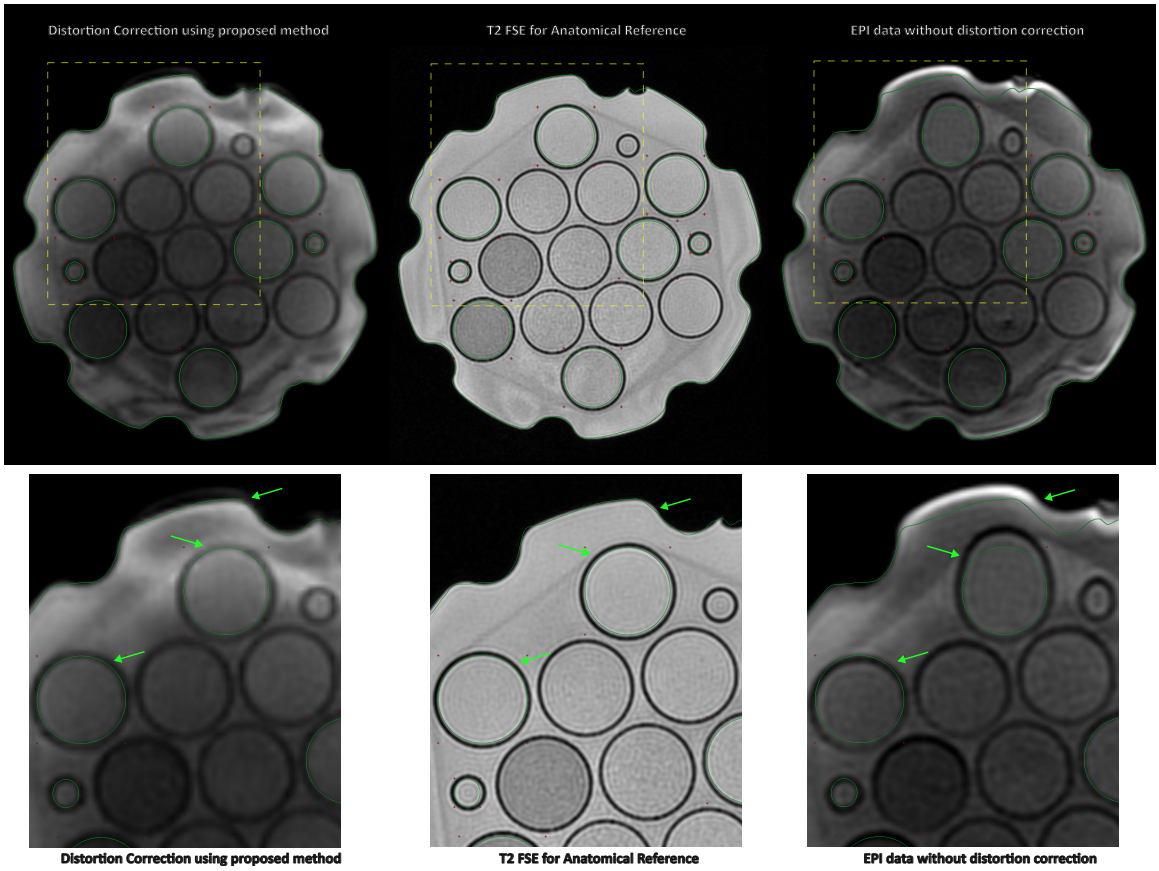

Figure 2: (Top Row) *Left.* Distortion corrected image using proposed method. *Middle.* T2-w FSE MRI for structural reference. *Right.* Uncorrected EPI data. The boundary of the phantom and some spheres inside it are marked using green boundaries. (Bottom Row) The zoomed in version of the top row image in yellow rectangles are shown here. The impact of distortion correction and its accuracy is pointed out by green arrows and boundary markers.

slice-slice variations. In Figure 5 notice that extreme distortion with signal pile-up noticed in forward and reverse polarity DWI data has been effectively restored in proposed solution; without any non-physical wraps of tissue and maintain the texture , contrast and preserves local signal consistency in hitherto region of signal pileup. Figure 6 demonstrates the effectiveness of the proposed approach in ability to maintain structural fidelity of in pelvis regions (consisting of prostate and ano-rectal assessment regions). (a. prostate, b-rectal regionion). This is important to ensure accurate assessment of cancer and other pathologies in pelvis region

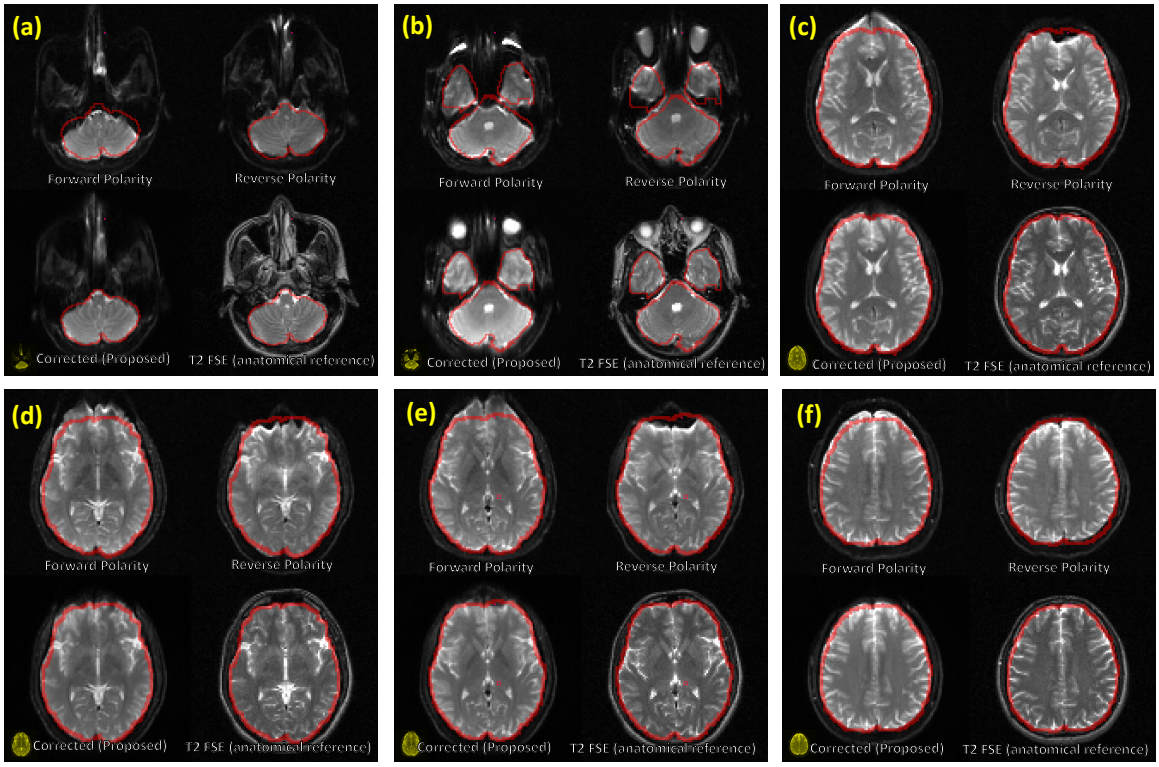

Figure 3: Performance of the proposed method for six different axial slices are shown here. For each example T2FSE MRI serving as anatomical reference is shown. The red delineation is performed to track the boundary of brain in T2FSE MRI. Post proposed correction, the distortion has been corrected across brain regions as sinus, eye balls (refer Figure 3(b)).

4. Conclusion

In this work, we present a model-based approach to correct distortions in EPI MR images. The method uses both forward and reverse phase-encoding acquisitions. A deep learning (DL) model estimates the field inhomogeneity, which is then used to construct an encoding matrix that relates the observed distorted signal to the distortion-free image. An unrolled DL-based reconstruction framework is applied to recover the distortion-free image. The proposed method demonstrated strong generalization across phantom and in-vivo EPI MRI data from multiple anatomies. Future work will focus on evaluating the method on larger and more diverse datasets and conducting reader studies to incorporate expert assessment.

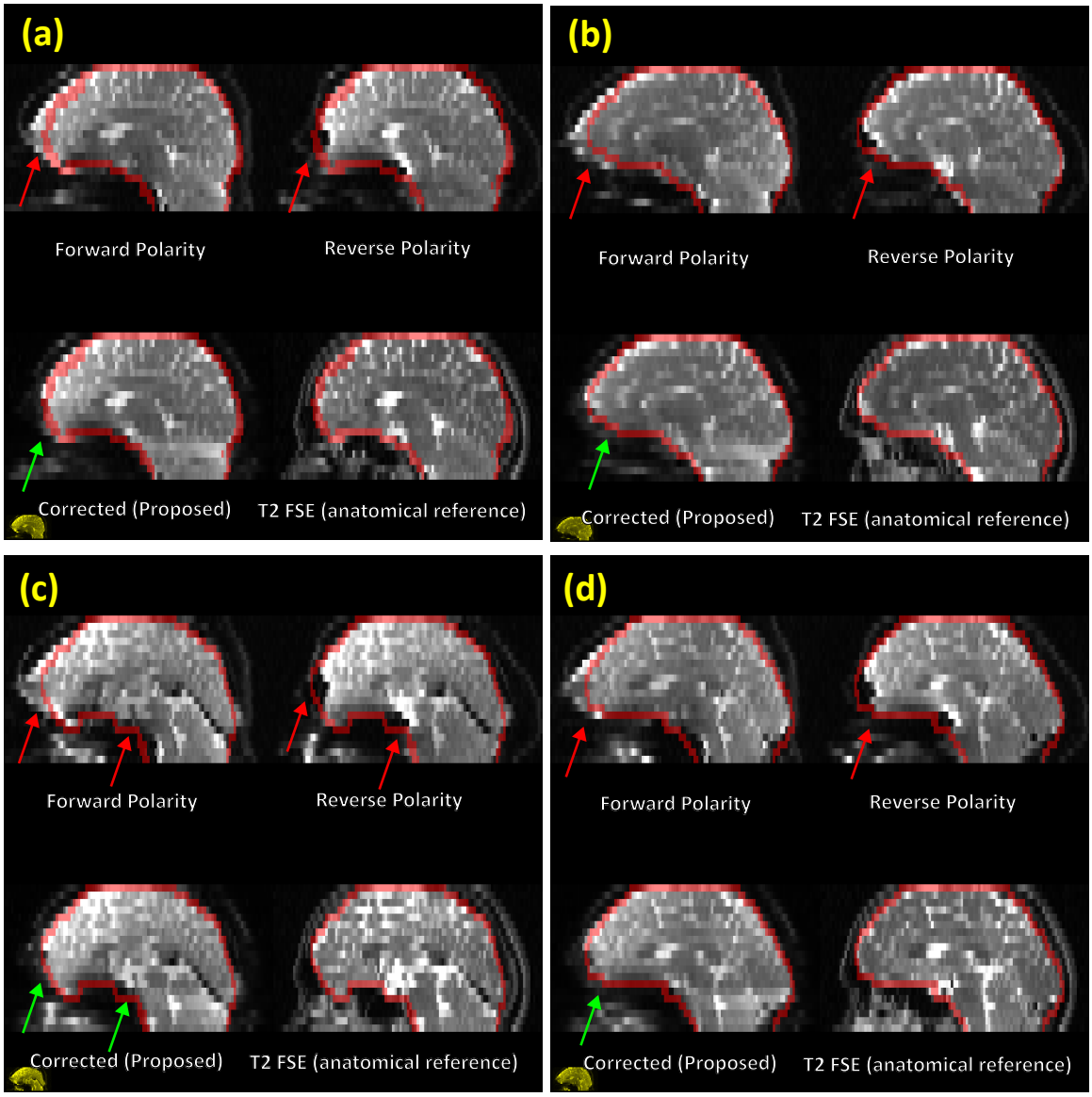

Figure 4: Similar analysis as mentioned in Figure 4 has been done here for the Sagittal view. In this view, the correction around sinus regions is prominent. The high distortion regions are pointed out by red arrows. Post correction using proposed method, the restored alignment with the T2FSE MRI is indicated by green arrows.

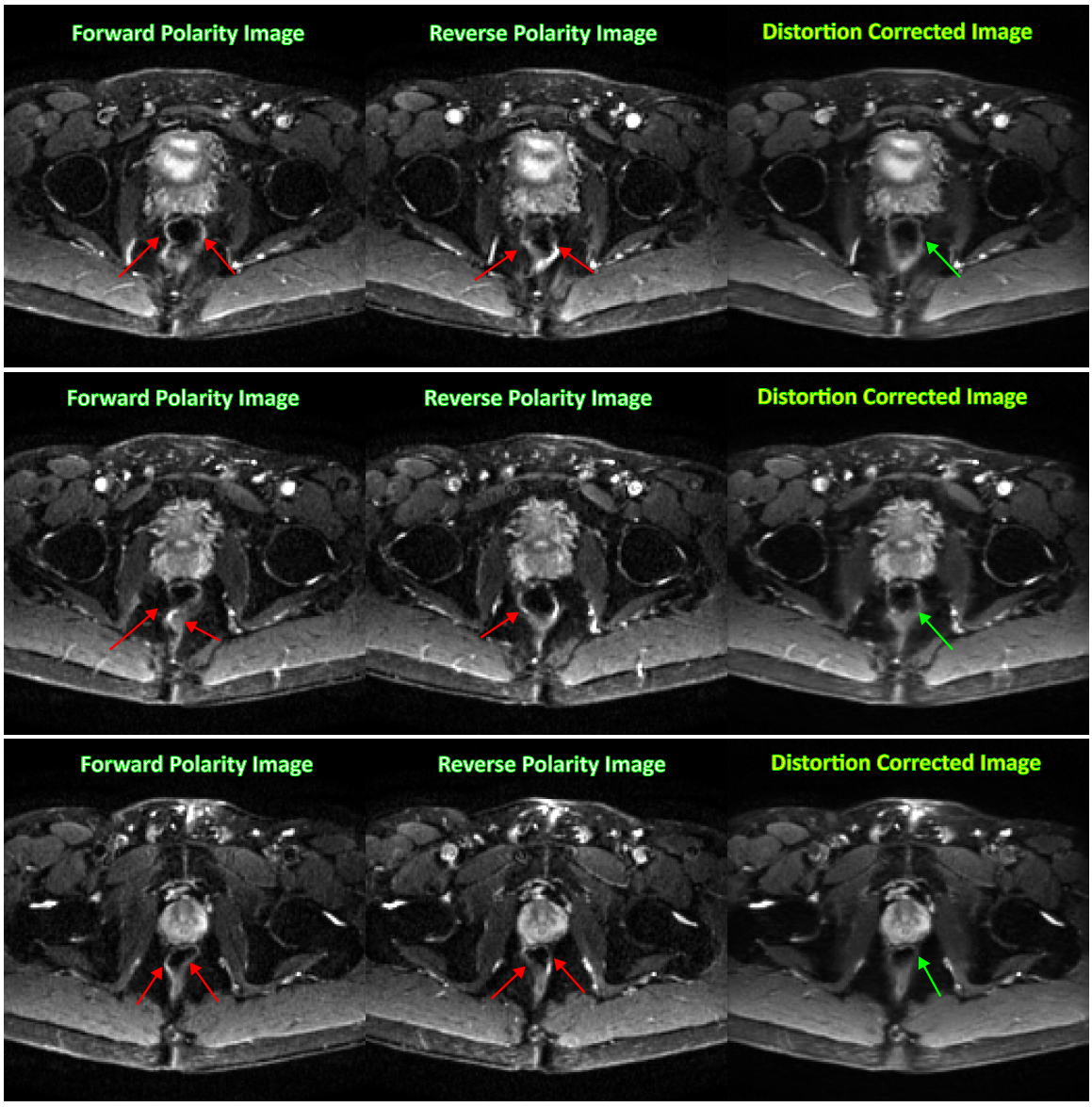

Figure 5: The impact of distortion correction using the proposed method for prostate EPI MR image is shown here. For the three examples (in each row), the red arrows indicate the high distortions in rectal region (high susceptibility area). Post correction using proposed method, the structures are restored with good effect (shown by green arrows).

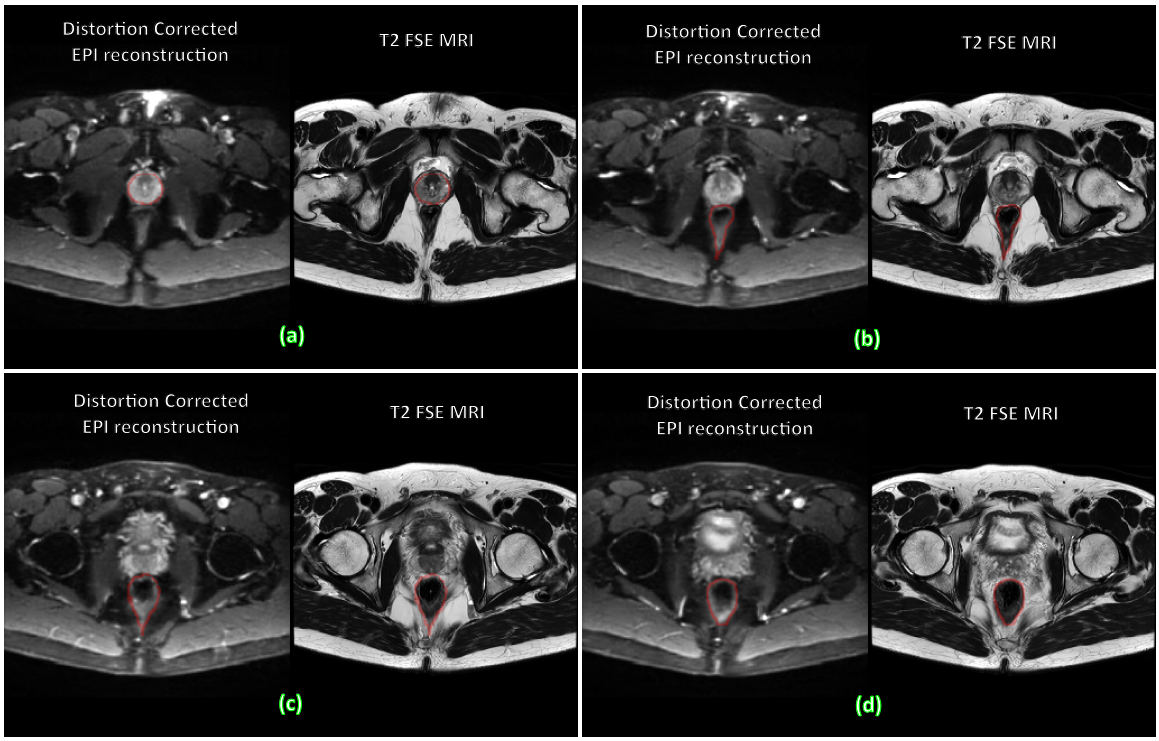

Figure 6: The distortion corrected prostate EPI data is compared against corresponding T2-w FSE data to conform proper alignment post correction using proposed method. Dileneations around the rectal region and prostate galnd was performed on T2-w FSE data. Results show high degree of co-alignment between distortion corrected EPI data and T2 FSE.

References

Eirikur Agustsson and Radu Timofte. NTIRE 2017 Challenge on Single Image Super-Resolution: Dataset and Study. In *IEEE Conference on Computer Vision and Pattern Recognition Workshops (CVPRW)*, July 2017.

Jesper LR Andersson, Stefan Skare, and John Ashburner. How to correct susceptibility distortions in spin-echo echo-planar images: application to diffusion tensor imaging. *Neuroimage*, 20(2):870–888, 2003.

Amir Beck and Marc Teboulle. A fast iterative shrinkage-thresholding algorithm for linear inverse problems. *SIAM Journal on Imaging Sciences*, 2(1):183–202, 2009. doi: 10.1137/080716542.

Matt A. Bernstein, Kevin F. King, and Xiaohong Joe Zhou. *Handbook of MRI Pulse Sequences*. Academic Press, 2004.

Robert W. Brown, Y.-C. Norman Cheng, E. Mark Haacke, Michael R. Thompson, and Ramesh Venkatesan. *Magnetic Resonance Imaging: Physical Principles and Sequence Design*. Wiley-Blackwell, 2 edition, 2014.

H. Chang and J. Michael Fitzpatrick. A technique for accurate magnetic resonance imaging in the presence of field inhomogeneities. *IEEE Transactions on Medical Imaging*, 11(3):319–329, 1992. doi: 10.1109/42.158935.

Patrick L. Combettes and Valérie R. Wajs. Signal recovery by proximal forward-backward splitting. *Multiscale Modeling & Simulation*, 4(4):1168–1200, 2005. doi: 10.1137/050626090.

Alfredo De Goyeneche Macaya, Shreya Ramachandran, Ke Wang, Ekin Karasan, Joseph Y Cheng, Stella X Yu, and Michael Lustig. Resonet: Noise-trained physics-informed mri off-resonance correction. *Advances in Neural Information Processing Systems*, 36:14192–14203, 2023.

Nuowei Ge, Qinqin Yang, Zejun Wu, Jianfeng Bao, Zhigang Wu, Congbo Cai, and Shuhui Cai. Dynamic distortion correction of me-epi using learning-based single-scan multi-echo blip up-down acquisition (me-buda). In *Proceedings of the 2024 ISMRM & ISMRT Annual Meeting & Exhibition*, Singapore, May 2024. International Society for Magnetic Resonance in Medicine. URL https://archive.ismrm.org/2024/2639_Knqkt7Pk3.html. Abstract #2639; Session D-02: Artifacts Correction & Mitigation.

Dominic Holland, Joshua M. Kuperman, and Anders M. Dale. Efficient correction of inhomogeneous static magnetic field-induced distortion in echo planar imaging. *NeuroImage*, 50(1):175–183, 2010. ISSN 1053-8119. doi: https://doi.org/10.1016/j.neuroimage.2009.11.044. URL https://www.sciencedirect.com/science/article/pii/S1053811909012294.

Peter Jezzard and Robert S. Balaban. Correction for geometric distortion in echo planar images from b_0 field variations. *Magnetic Resonance in Medicine*, 34(1):65–73, 1995. doi: 10.1002/mrm.1910340111.

R Marc Lebel. Performance characterization of a novel deep learning-based mr image reconstruction pipeline. *arXiv preprint arXiv:2008.06559*, 2020.

Bee Lim, Sanghyun Son, Heewon Kim, Seungjun Nah, and Kyoung Mu Lee. Enhanced deep residual networks for single image super-resolution. In *Proceedings of the IEEE conference on computer vision and pattern recognition workshops*, pages 136–144, 2017.

Paul S. Morgan, Richard W. Bowtell, D. J. O. McIntyre, and B. S. Worthington. Correction of spatial distortion in epi due to inhomogeneous static magnetic fields using the reversed gradient method. *Journal of Magnetic Resonance Imaging*, 19(4):499–507, 2004. doi: 10.1002/jmri.20032.

Matthew J Muckley, Benjamin Ades-Aron, Antonios Papaioannou, Gregory Lemberskiy, Eddy Solomon, Yvonne W Lui, Daniel K Sodickson, Els Fieremans, Dmitry S Novikov, and Florian Knoll. Training a neural network for gibbs and noise removal in diffusion mri. *Magnetic resonance in medicine*, 85(1):413–428, 2021.

Patrice Munger, Gerard R Crelier, Terry M Peters, and G Bruce Pike. An inverse problem approach to the correction of distortion in epi images. *IEEE Transactions on Medical Imaging*, 19(7):681–689, 2000.

Klaas P Pruessmann, Markus Weiger, Markus B Scheidegger, and Peter Boesiger. Sense: sensitivity encoding for fast mri. *Magnetic Resonance in Medicine: An Official Journal of the International Society for Magnetic Resonance in Medicine*, 42(5):952–962, 1999.

Uten Yarach, Myung-Ho In, Itthi Chatnuntawech, Berkin Bilgic, Frank Godenschweger, Hendrik Mattern, Alessandro Sciarra, and Oliver Speck. Model-based iterative reconstruction for single-shot epi at 7 t. *Magnetic resonance in medicine*, 78(6):2250–2264, 2017.

Kylie Yeung, Christine Tobler, Rolf F Schulte, Benjamin White, Anthony McIntyre, Sébastien Serres, Peter Morris, Dorothee Auer, Fergus V Gleeson, Damian J Tyler, et al. Algebraic methods and computational strategies for pseudoinverse-based mr image reconstruction (pinv-recon). *Scientific Reports*, 15(1):37997, 2025.

Abdallah Zaid Alkilani, Tolga Çukur, and Emine Ulku Saritas. Fd-net: An unsupervised deep forward-distortion model for susceptibility artifact correction in epi. *Magnetic Resonance in Medicine*, 91(1):280–296, 2024.

Yulun Zhang, Kunpeng Li, Kai Li, Lichen Wang, Bineng Zhong, and Yun Fu. Image super-resolution using very deep residual channel attention networks. In *Proceedings of the European conference on computer vision (ECCV)*, pages 286–301, 2018.

Appendix A. Step-size selection ($\tau = 1$)

We reconstruct the image by minimizing a composite objective composed of a smooth data term and a regularizer:

$$f(x) + \lambda\, R(x). \tag{9}$$

This objective arises from the signal model, where the measured k-space data and the unknown image are related by: $y = E(\Delta B_0)\, x$. We define the smooth data term and the encoding operator as:

$$f(x) \;=\; \left\| y - E(\Delta B_0)\, x \right\|_2^2, \tag{10}$$

where, $E(\Delta B_0) = \mathbf{F}_{2\mathrm{D}} \odot \mathbf{\Psi}(\Delta B_0)$, with the off-resonance phase mask being unimodular: $\left|\mathbf{\Psi}_{ij}\right| = 1$. The gradient of the data term is:

$$\nabla f(x) \;=\; 2\, E(\Delta B_0)^H \left(E(\Delta B_0)\, x - y\right). \tag{11}$$

Hence, the gradient is L_f-Lipschitz with:

$$L_f \;=\; 2 \left\| E(\Delta B_0)^H E(\Delta B_0) \right\|_2 \;=\; 2 \left\| E(\Delta B_0) \right\|_2^2. \tag{12}$$

In the forward–backward (proximal-gradient) framework, a fixed step size is admissible when: $\tau \in (0,\, 2/L_f)$, while in the standard proximal-gradient/FISTA analysis a conservative rule is used: $\tau \leq \frac{1}{L_f}$ (Combettes and Wajs, 2005; Beck and Teboulle, 2009). In this work, we adopt the fixed choice:$\tau = 1$, without per-dataset verification of L_f, justified by the structure of the encoding operator. Specifically, we use the unitary Cartesian DFT convention for $\mathbf{F}_{2\mathrm{D}}$: $\left\| \mathbf{F}_{2\mathrm{D}} \right\|_2 = 1$, and a sample/voxel-dependent unimodular phase mask $\mathbf{\Psi}$, which in typical Cartesian acquisitions yields:$\left\| E(\Delta B_0) \right\|_2 \approx 1$, so that: $L_f \approx 2$, and: $\tau = 1 \in (0,\, 2/L_f)$ or lies near the admissible boundary. If $\tau = 1$ were empirically at the boundary (i.e., $L_f \simeq 2$), we rely on standard safeguards to preserve monotonic decrease and convergence guarantees, namely mild damping:$\tau = 0.99$ or an optional backtracking line-search as in (Beck and Teboulle, 2009), while keeping a fixed-step implementation consistent with the physics encoded in $E(\Delta B_0)$.

Appendix B. EPI Distortion Correction in NIST Diffusion Phantom

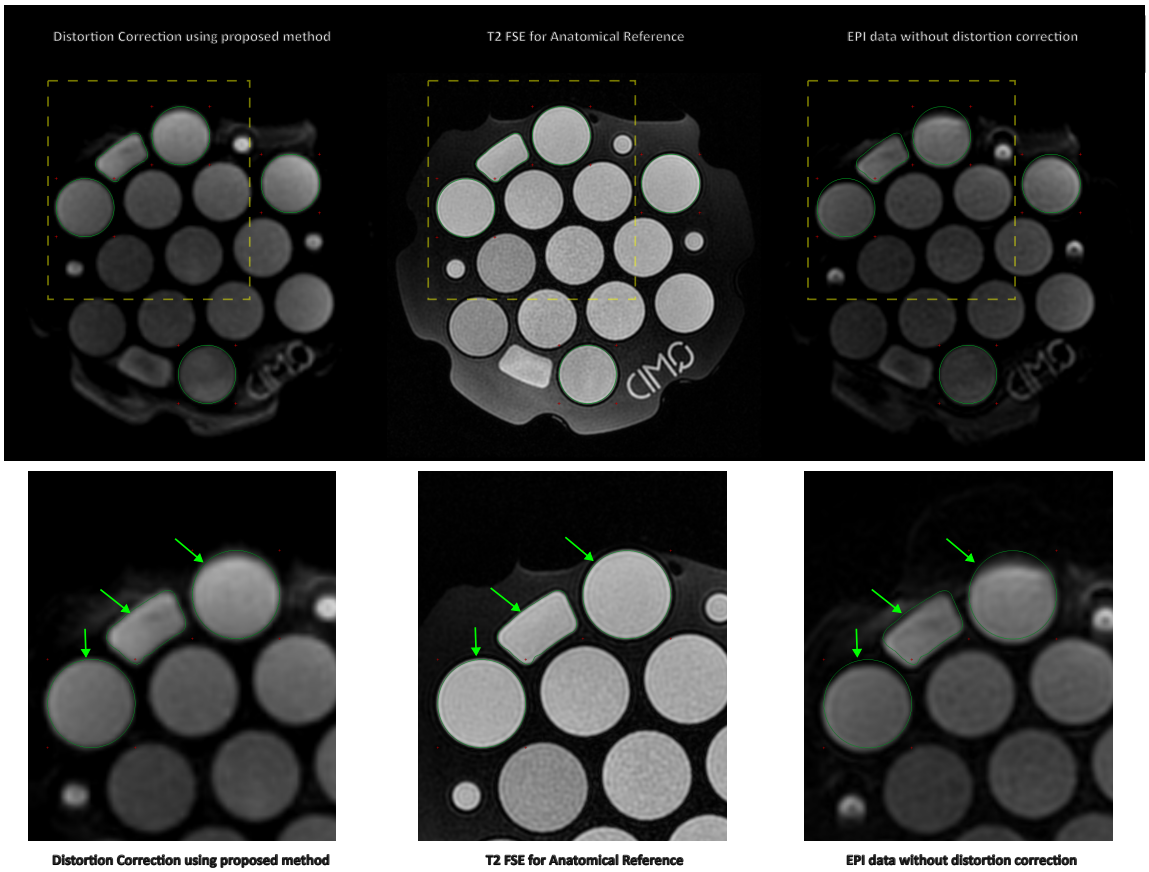

Figure 7: (Top Row) *Left.* Distortion corrected image using proposed method. *Middle.* T2-w FSE MRI for structural reference. *Right.* Uncorrected EPI data. The boundary of the phantom and some spheres inside it are marked using green boundaries. (Bottom Row) The zoomed in version of the top row image in yellow rectangles are shown here. The impact of distortion correction and its accuracy is pointed out by green arrows and boundary markers.